High-throughput screening for biomedical applications in a Ti-Zr-Nb alloy system through masking co-sputtering

Xue-Hui Yan, Jiang Ma and Yong Zhang

Citation: SCIENCE CHINA Physics, Mechanics & Astronomy **62**, 996111 (2019); doi: 10.1007/s11433-019-9387-7

View online: http://engine.scichina.com/doi/10.1007/s11433-019-9387-7

SCIENCE CHINA
Physics, Mechanics & Astronomy

SCIENCE CHINA
Physics, Mechanics & Astronomy

•Article•

September 2019 Vol. 62 No. 9: 996111
https://doi.org/10.1007/s11433-019-9387-7

High-throughput screening for biomedical applications in a Ti-Zr-Nb alloy system through masking co-sputtering

Xue-Hui Yan[1], Jiang Ma[2], and Yong Zhang[1*]

[1] *Beijing Advanced Innovation Center of Materials Genome Engineering, State Key Laboratory for Advanced Metals and Materials, University of Science and Technology Beijing, Beijing 100083, China;*
[2] *College of Mechatronic and Control Engineering, Shenzhen University, Shenzhen 518060, China*

Received January 28, 2019; accepted March 7, 2019; published online April 25, 2019

A method of co-sputtering deposition combined with physical masking was applied to the parallel preparation of a ternary Ti-Nb-Zr system alloy. Sixteen independent specimens with varying compositions were obtained. Their microstructure, phase structure, Young's modulus, nanoindentation hardness, and electrochemical behavior in a phosphate buffer solution (PBS) were studied in detail. It was revealed that the Ti-Zr-Nb alloys possess a single BCC structure. As confirmed via nanoindentation tests, the Young's modulus of the specimens ranged from 80.3 to 94.8 GPa and the nanoindentation hardness ranged from 3.6 to 5.0 GPa. By optimizing the composition of the specimens, the $Ti_{34}Zr_{52}Nb_{14}$ alloy was made to possess the lowest modulus in this work (76.5 GPa). Moreover, the $Ti_{34}Zr_{52}Nb_{14}$ alloy showed excellent corrosion resistance in PBS without any tendency for pitting at anodic potentials up to 1 V_{sce}. These preliminary advantages offer the opportunity to explore new orthopedic implant alloys based on Ti-Zr-Nb alloys. Moreover, this work provides an effective method for the parallel preparation of biomedical alloys.

high-throughput, biomedical materials, co-sputtering, physical mask, Young's modulus

PACS number(s): 61.43.–j, 61.43.Dq, 61.46.–w, 62.20.–x, 62.20.Dc, 87.68.+z

Citation: X.-H. Yan, J. Ma, and Y. Zhang, High-throughput screening for biomedical applications in a Ti-Zr-Nb alloy system through masking co-sputtering, Sci. China-Phys. Mech. Astron. **62**, 996111 (2019), https://doi.org/10.1007/s11433-019-9387-7

1 Introduction

Metallic materials have been widely applied in the synthesis of biomedical implant materials owing to their advantageous processing and mechanical properties such as high strength, high fatigue strength, and good toughness. Typically, metallic materials are used for knee joints, bone plates, and dental materials [1-3]. For implants, both biocompatibility and mechanical compatibility are critical factors that determine the usability of the material. In general consideration, implants should have hardness and Young's modulus that are comparable to those of bone so as to avoid the "stress shielding" effect [4].

Titanium alloys are a class of biocompatible implant materials with low densities and Young's moduli. They have gradually become the preferred materials for tissue repair and replacement [5]. Currently, titanium alloys are designed using non-toxic components such as Nb, Zr, Ta, Sn, In, and Mo, which tend to form a single BCC phase in the structure [6-12]. Compared with the classic early biomedical materials, including Ti-6Al-4V (Young's modulus of 110 GPa), CoCrMo (Young's modulus of 230 GPa), and 316L SS (Young's modulus of 210 GPa) [13-16], the new type of titanium alloys feature improved mechanical properties and corrosion resistance. There are many common systems, such as Ti-Nb-Zr, Ti-Ta-Nb, Ti-Zr-Ta-Nb, Ti-Mo-Zr-Fe, and Ti-

*Corresponding author (email: drzhangy@ustb.edu.cn)

Nb-Zr-Sn, with Young's moduli in the range 70-100 GPa [17-21]. Recently, bulk metallic glass (BMG) has also been considered as a potential biomedical material owing to its excellent corrosion resistance, large breaking strength, low Young's modulus (comparable to that of bone), and good biocompatibility [22-24].

From the perspective of mixing entropy, materials can be divided into three classes [25]: (1) low entropy alloys with one or two components, (2) medium entropy alloys with three or four components, and (3) high-entropy materials with no less than five components. Among them, a solid-solution structure can be formed when the number of components is greater than three. This is mainly because the mixing entropy can gradually compete with the strong chemical bonds between elements. Therefore, the concept of configuration-entropy alloys (CEAs), which refers to multi-component materials with strong configuration entropy, is of interest, particularly when used in combination with biomedical materials such as TiZrNbTa, TiZrNbTaMo, and HfNbTiZr [16,26,27]. Such materials generally possess high compressive strength, excellent corrosion resistance in the simulated physiological medium, as well as Ti-comparable biocompatibility.

Owing to the limitations of research methods, few specific compositions can be obtained from a set of experiments using conventional methods. For biomedical materials, the obtained Young's modulus value is a relatively low value in a small composition region, rather than the lowest value of a global system. Therefore, a traditional "trial and error" method inevitably causes incompleteness and contingency in research results. Furthermore, new research on CEAs is now being conducted in relation to biomedical alloys. However, the non-linear relationship between mixing entropy and performance makes the screening process more difficult. In this case, parallel preparation is an effective way to obtain a composition with a low Young's modulus in a larger composition region. As reported, compositional gradient materials have been prepared by multi-target co-sputtering. A high composition coverage has been obtained and the range of element contents varied from ~3 at.% to 90 at.% [28,29]. If the method can be applied to the parallel preparation of biomedical alloys, it will be possible to screen materials over a larger range of compositions.

In combining the CEA concept with biomedical materials, the Ti-Zr-Nb ternary system was selected as the basic composition in this work. On the basis of multi-target co-sputtering, an auxiliary physical mask was used to facilitate the preparation of compositional gradient materials and 16 independent specimens were obtained. To this end, the purpose of this work was to use the method to achieve parallel preparation of Ti-Zr-Nb alloys and to identify the low modulus components of the Ti-Zr-Nb system. Initially, the microstructure and phase structure of the 16 specimens were characterized. Next, the fundamental properties were studied, including Young's modulus, nanoindentation hardness, and electrochemical behavior. The trend in the Young's modulus was fitted using three-dimensional (3D) surface maps and contour maps. Finally, the validity of semi-empirical criteria for phase selection was examined in terms of "Ω-δ" rules and valence electron concentration (VEC).

2 Materials and methods

The method combining co-sputtering deposition with physical masking was applied to the parallel preparation of ternary Ti-Nb-Zr alloys. Using Ti, Zr, and Nb (purity <99.9% in weight percentage) as raw materials, three targets with a diameter of 50 mm and thickness of 3 mm were fabricated by a hot-pressing process. The Ti target was under direct current (DC) power (100 W), the Nb target was under radio frequency (RF) power (80 W), and the Zr target under DC power (80 W). A P-type Si (100) wafer covered by a 300-nm silicon-oxide coating was selected as a substrate for this work. The wafer was disc-shaped with a diameter of 15.24 cm and a thickness of 625 nm. Prior to deposition, the base pressure was maintained at 6×10^{-4} Pa. Subsequently, argon was introduced into the chamber at a flow rate of 50 sccm, and the chamber pressure was maintained at 0.5 Pa for deposition. Before formal deposition, the targets were pre-sputtered with the source shutter closed for 5 min. The deposition time was 60 min and the working distance was 50 mm.

Different from conventional co-sputtering, the substrate stage was fixed during deposition. Variations in the relative position between the targets and substrate can cause non-uniformity of deposition. Utilizing the differences in deposition density on the substrate, compositional gradient materials were obtained. Figure 1(a) shows the deposition process. A 16-grid stainless steel shadow mask (120 mm×120 mm×0.2 mm) prepared by laser was covered onto the substrate. As such, 16 independent specimens with different compositions were obtained. The squares on each grid were 10 mm×10 mm, and the spacing between adjacent squares was 20 mm. For the shadow mask, there were four grids in each horizontal and vertical direction. With the horizontal (H) and vertical (V) axes as references, each specimen is named in the form V-H (V ranging 1 to 4, H ranging 1 to 4), as shown in Figure 1(b).

Determination of surface morphology and cross-sectional microstructure were carried out on a field-emission scanning electron microscopy (SEM, Auriga Field Emission Scanning Electron Microscope, Carl Zeiss, Germany) equipped with an energy dispersive X-ray spectrometer (EDX). The final average compositions of the alloys were confirmed with EDX at 15 KeV. To ensure the accuracy of the measured

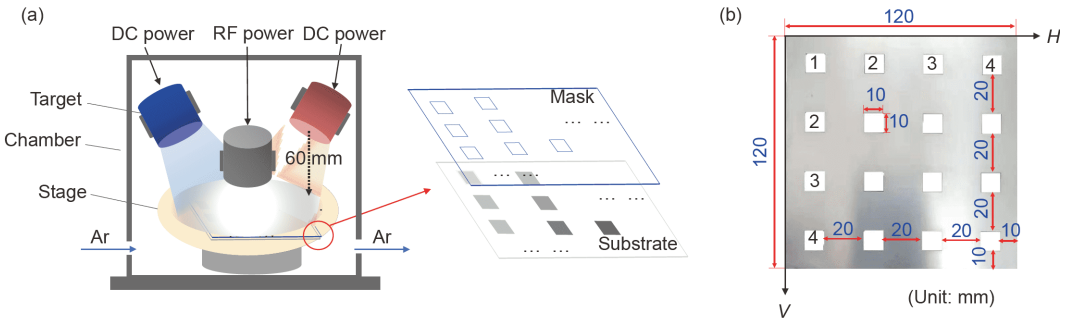

Figure 1 (Color online) (a) Schematic diagram of parallel preparation for a ternary Ti-Nb-Zr system and (b) the shadow mask used in the present work.

composition, each sample was tested three times in different regions. Three-dimensional topography and surface roughness were characterized using an atomic force microscope (AFM, Veeco DI-3100, USA). The scanning region was about 5 μm×5 μm.

To characterize the hardness and Young's modulus of the Ti-Zr-Nb alloys, nanoindentation tests were carried on the films using a Berkovich triangular pyramid indenter with a tip radius of 20 nm. The Poisson's ratio and elastic modulus of the indenter tip were 0.07 and 1.141×10^6 MPa, respectively. Indentation was performed in the continuous stiffness mode (CSM) with an indentation load of 500 mN and surface approach velocity of 10 nm/s. To ensure the accuracy of the tested point and avoid any influence of the substrate, the valid indentation depth was maintained at 10% of the film thickness. Each sample was tested at six points and the distance between each indentation was 1000 nm. The change trends in hardness and Young's modulus of the 16 specimens were fitted using 3D surface maps and contour maps.

The crystal structures of the Ti-Zr-Nb alloy films were analyzed by a glancing-incidence (1°) X-ray diffractometer (XRD, BRUKERD8 Discover, Germany) using Cu Kα radiation. The continuous scanning mode was used to scan in the range 10°-100° at a scanning rate of 4°/min. On the basis of the XRD patterns, the lattice parameters of the crystalline phase were determined by $d_{hkl}= a/\sqrt{h^2+k^2+l^2}$, with the Bragg equation $2d_{hkl}\sin\theta = \lambda$.

The corrosion behavior of the alloy was evaluated by electrochemical measurements. A phosphate buffer solution (PBS) was selected as a corrosive solution to preliminarily assess corrosion resistance in a physical environment. A cubic specimen with dimensions of 5 mm×5 mm×1 mm was tested at room temperature. The electrochemical measurements were conducted in a three-electrode cell with platinum foil as the counter electrode and saturated calomel as the reference electrode using a Model 2273 electrochemical workstation (EG&G Princeton Applied Research). Prior to the measurements, the specimens were immersed in an electrolyte for 2 h to attain a stable state of open circuit potential (OCP). A polarization test was conducted in the range −0.5 to 1 V at a scanning rate of 0.167 mV/s.

3 Results

3.1 Composition characterization

As characterized by EDX analysis, the final chemical compositions (average values for triplicate measurements) of the 16 specimens are shown in Table 1. For the sake of simplicity, the compositional distribution is depicted in a ternary compositional map, as shown in Figure 2. As indicated, the contents of the component elements of the alloys were located in the range 15 at.%-71 at.% (Ti), 21 at.%-70 at.% (Zr), and 5 at.%-43 at.% (Nb). The entropies of mixing (ΔS_{mix}) of the Ti-Zr-Nb alloys were calculated using the following equation, which is described according to Boltzmann's hypothesis [30]:

$$\Delta S_{\mathrm{mix}} = -R\sum_{i=1}^{n}(c_i \ln c_i),$$

Table 1 Chemical compositions of Ti-Nb-Zr alloys

Number (*V-H*)	Ti (at.%)	Zr (at.%)	Nb (at.%)	Composition
1-1	70.75	21.68	7.57	$Ti_{71}Zr_{22}Nb_7$
1-2	60.57	25.44	13.98	$Ti_{61}Zr_{25}Nb_{14}$
1-3	45.21	27.23	27.56	$Ti_{45}Zr_{27}Nb_{28}$
1-4	31.42	25.88	42.70	$Ti_{31}Zr_{26}Nb_{43}$
2-1	59.47	32.19	8.34	$Ti_{60}Zr_{32}Nb_8$
2-2	47.34	39.52	13.14	$Ti_{47}Zr_{40}Nb_{13}$
2-3	35.84	41.23	22.94	$Ti_{36}Zr_{41}Nb_{23}$
2-4	26.99	37.73	35.28	$Ti_{27}Zr_{38}Nb_{35}$
3-1	42.39	51.17	6.44	$Ti_{42}Zr_{51}Nb_7$
3-2	35.57	54.13	10.30	$Ti_{36}Zr_{54}Nb_{10}$
3-3	25.90	56.24	17.86	$Ti_{26}Zr_{56}Nb_{18}$
3-4	19.95	55.17	24.78	$Ti_{20}Zr_{55}Nb_{25}$
4-1	29.48	64.74	5.78	$Ti_{29}Zr_{65}Nb_6$
4-2	23.76	68.82	7.43	$Ti_{24}Zr_{69}Nb_7$
4-3	19.05	69.80	11.14	$Ti_{19}Zr_{70}Nb_{11}$
4-4	15.34	67.57	17.09	$Ti_{15}Zr_{68}Nb_{17}$

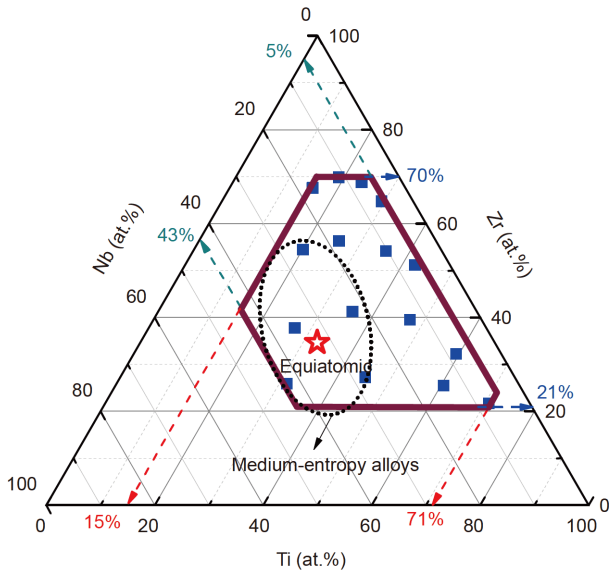

Figure 2 (Color online) Schematic location of Ti-Zr-Nb alloys in a ternary compositional map.

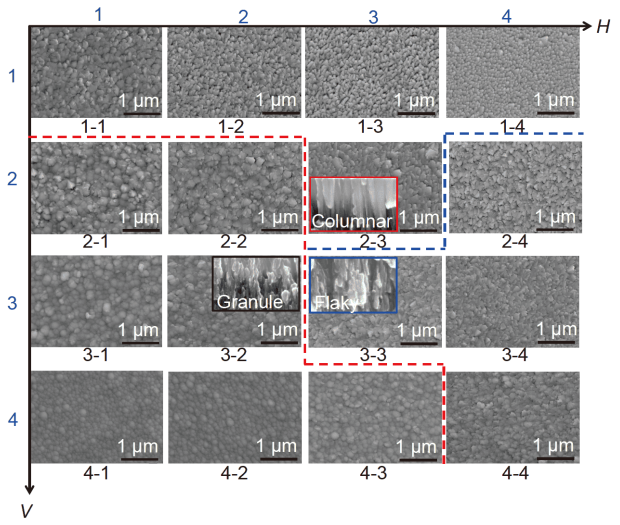

Figure 3 (Color online) SEM images of the deposited Ti-Zr-Nb alloys taken from the surface and cross-section.

where c_i is mole percent of a component, $\sum_{i=1}^{n} c_i = 1$, and R (= 8.314 J/K/mol) is the gas constant. The values of ΔS_{mix} for the ternary Ti-Zr-Nb alloys with different compositions ranged from 0.77 to 1.1R. This indicates that the Ti-Zr-Nb system alloys belong to the low-entropy and medium-entropy alloy categories. Theoretically, for a given alloy system, the ΔS_{mix} value of a composition with an equiatomic ratio would be the maximum. As such, alloys with medium-entropy were distributed around the equiatomic ternary Ti-Zr-Nb alloy, which is noted in Figure 2 as a five-pointed star.

3.2 Microstructure characterization

Figure 3 shows SEM images of the Ti-Zr-Nb alloys, wherein the arrangement of the 16 images corresponds to the specimen number of the physical mask. As indicated, the morphologies of the alloys somewhat varied with composition. The images can be loosely divided into three kinds of topographic features, which are separated by colored lines: 1) pyramid-shaped surface features having the cross-section of a columnar structure, 2) spherical-shaped surface features having the cross-section of a granular structure, and 3) faceted surface features having the cross-section of a lamellar structure. The surfaces and 3D morphologies of three typical Ti-Zr-Nb alloys were also characterized by AFM, as shown in Figure 4. As characterized by AFM, the morphologies aligned well with the SEM images. For the three typical surfaces, variation can be observed in their 3D morphologies. For pyramid-shaped surface features, shown in Figure 4(a), a 3D characteristic of uniform and fine needle

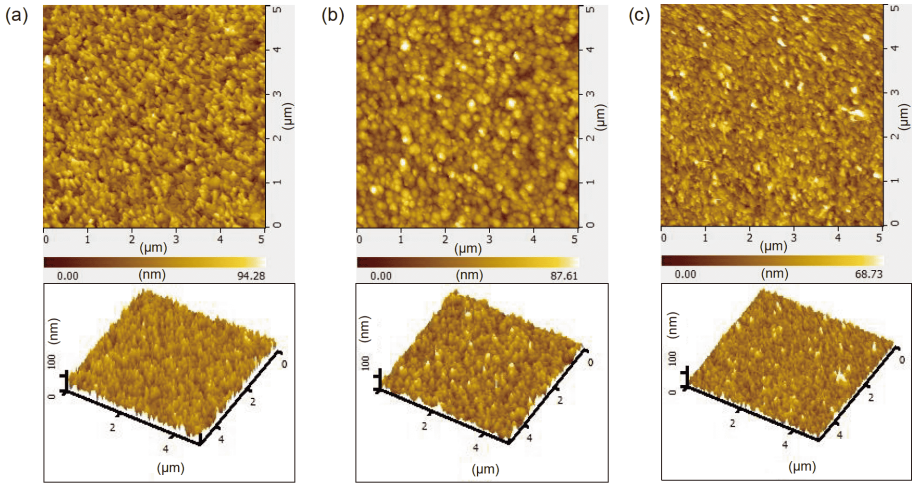

Figure 4 (Color online) Plane and 3D morphologies of three typical Ti-Zr-Nb alloy surfaces. (a) Spherical-shaped surface feature, (b) pyramid-shaped surface feature, (c) faceted surface feature.

shapes is exhibited, although the needle-shaped particles gradually became coarse (Figure 4(b)). For faceted surface features, the 3D surface topography became flatter. Moreover, the scale in Figure 4 shows the change in surface fluctuation. The alloys showed a particular surface feature with low surface roughness. The roughness values for the images shown in Figure 4 are 11.92, 10.99, and 8.15 nm, respectively.

The average thickness of the Ti-Zr-Nb alloys was 1.16 μm. Owing to differences in deposition density, the thicknesses of the alloys were not uniform. Overall, the alloys with faceted surface features were thinner than those with the other surface features. This is mainly because these specimens were close to the Nb deposition source, which was equipped with an RF power source and had a low deposition yield. On average, the thickness was ~15.6% less than that of the pyramid- and spherical-shaped alloys. It can be inferred that the deposition yield also contributed to the differences in morphological features. Under higher deposition yield, the adatom mobility on the growing film can be enhanced to allow for diffusion of underlying crystals or grains. As the deposition yield increases, the higher becomes the atomic mobility and the more complete is the columnar structure, as shown in the cross-section morphologies in Figure 3.

3.3 Young's modulus and hardness

The Young's modulus and indentation hardness (H_{IT}) of the Ti-Zr-Nb alloys were tested by nanoindentation. In general, these 16 specimens showed a low Young's modulus, ranging from 80.3 to 94.8 GPa. For the sake of clarity, the tested Young's modulus values were fitted to 3D surface maps and contour maps, as shown in Figure 5. Significantly, a low Young's modulus region is evident in Figure 5(a); this is basin-shaped and mainly covers specimens 2-2, 2-3, 3-2, 3-3, and 3-4 (in the form *V*-*H*). In Figure 5(b), the Young's modulus values are converted to a contour map. It is obvious that the specimens with lower Young's modulus values are concentrated in the region with *V* ranging from 2 to 3. The specific compositions of the five specimens with lower Young's moduli are given in Figure 5(c).

It is noteworthy that there is no obvious correlation between the trend in Young's modulus and the microstructures. This sequence is consistent with the idea that Young's modulus is not sensitive to microstructure. To determine whether a lower modulus composition existed in the blank

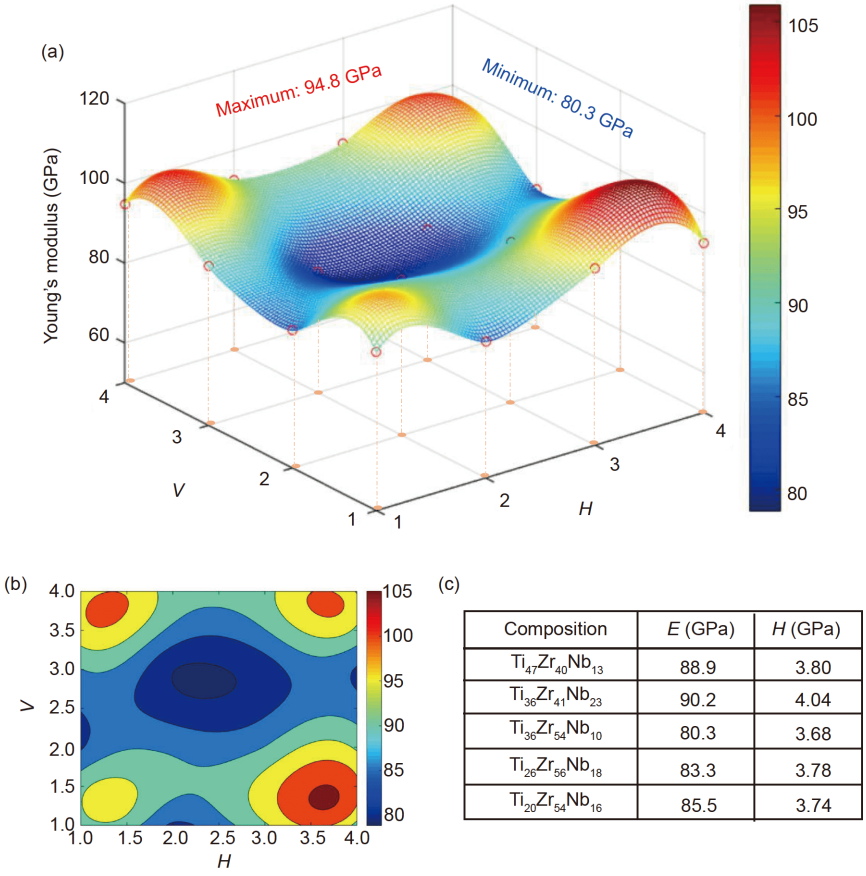

(c)

Composition	*E* (GPa)	*H* (GPa)
$Ti_{47}Zr_{40}Nb_{13}$	88.9	3.80
$Ti_{36}Zr_{41}Nb_{23}$	90.2	4.04
$Ti_{36}Zr_{54}Nb_{10}$	80.3	3.68
$Ti_{26}Zr_{56}Nb_{18}$	83.3	3.78
$Ti_{20}Zr_{54}Nb_{16}$	85.5	3.74

Figure 5 (Color online) Trend in Young's modulus of Ti-Zr-Nb alloys. (a) 3D surface map, (b) counter map, (c) specific values of specimens with lower Young's moduli.

areas between the specimens with lower Young's moduli, further optimization of the composition was conducted. The results show that the $Ti_{34}Zr_{52}Nb_{14}$ alloy possessed the lowest Young's modulus in this work. The Young's modulus and H_{IT} values were 76.5 and 3.8 GPa, respectively.

The indentation hardness of the Ti-Zr-Nb alloys ranged from 3.6 to 5.0 GPa, as shown in Figure 6. Overall, the change trend in indentation hardness was similar to that of the Young's modulus. For the sake of comparison, the H_{IT} values were converted into the equivalent Vickers hardness (H_v). H_{IT} values are derived from the formula

$$H_{IT}(\text{GPa}) = P / A_p,$$

where P is the indentation load and A_p is the projected contact area. For a Berkovich indenter, the ratio of the projected area (A_p) to the face area (A_s) is 0.9081. According to ISO 14577-1-2002, the relationship between H_v and H_{IT} can be approximated as H_v=0.9081H_{IT} [31]. As such, the H_v values of the Ti-Zr-Nb alloy films ranged from 3.3 to 4.5 GPa.

3.4 Phase structure analysis

Figure 7 shows the XRD patterns of the five Ti-Zr-Nb alloys with lower Young's moduli, as mentioned in the previous section. It is indicated that the specimens have a BCC phase structure. Overall, peak (110) is the main peak, with peaks (200) and (211) having less intensity. As shown in Figure 7, the Bragg angle shifts to a low value for specimens V=3 (3-1, 2, 3), indicating that the lattice parameter became slightly larger. The element contents are shown in Figure 8, and the inset shows the relative positions of the targets and specimens. Compared with specimens V=2 (2-2, 3), the content of Zr is significantly improved in V=3 (3-1, 2, 3) specimens, which were close to the Zr target. Typical parameters for the components are listed in Table 2. It shows that the lattice parameter of Zr is higher than those of Ti and Nb. Therefore, as the Zr content increases, the diffraction angle shifts to a lower 2θ angle, which is consistent with the larger lattice parameter at high Zr contents. The Nb element has a similar atom radius and lattice constant to β-Ti. As such, the change in Nb content does not have a significant effect on the lattice constant.

Combining $d_{hkl} = a / \sqrt{h^2+k^2+l^2}$ with the Bragg diffraction formula of $2d\sin\theta=\lambda$, the lattice constant (a) may be

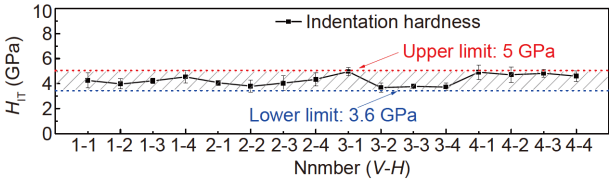

Figure 6 (Color online) Indentation hardness values of the 16 specimens tested.

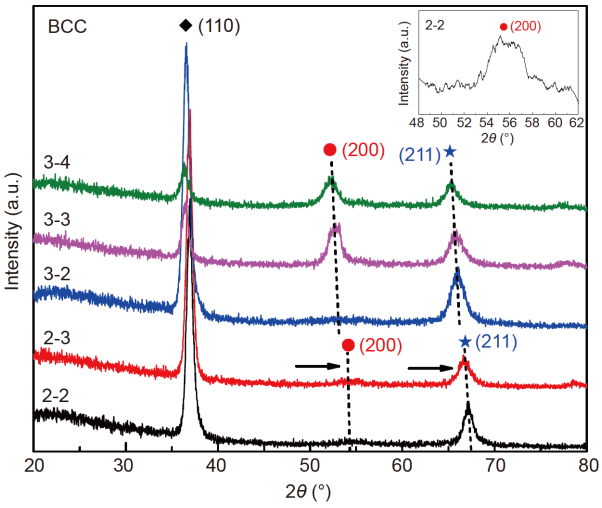

Figure 7 (Color online) XRD patterns of Ti-Zr-Nb alloys with lower Young's moduli: (2-2) $Ti_{47}Zr_{40}Nb_{13}$, (2-3) $Ti_{36}Zr_{41}Nb_{23}$, (3-2) $Ti_{36}Zr_{54}Nb_{10}$, (3-3) $Ti_{26}Zr_{56}Nb_{18}$, and (3-4) $Ti_{20}Zr_{54}Nb_{16}$.

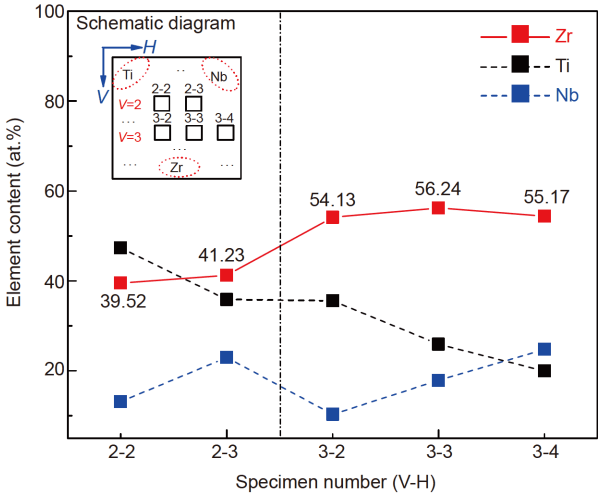

Figure 8 (Color online) Element contents of the Ti-Zr-Nb alloys with lower Young's moduli: (2-2) $Ti_{47}Zr_{40}Nb_{13}$, (2-3) $Ti_{36}Zr_{41}Nb_{23}$, (3-2) $Ti_{36}Zr_{54}Nb_{10}$, (3-3) $Ti_{26}Zr_{56}Nb_{18}$, (3-4) $Ti_{20}Zr_{54}Nb_{16}$.

Table 2 Selected parameters of the constituent elements of Ti-Zr-Nb[a)]

Element	Atomic radius r (nm)	Crystal structure	Lattice parameter a (nm)	Melting temperature T_m (K)	Valence electron concentration (VEC)
Ti	0.143	A2	0.32998	1941	4
Zr	0.16	A2	0.3609	2128	4
Nb	0.143	A2	0.33007	2750	5

a) Lattice parameter of BCC structure at high temperature.

expressed in the following form:

$$a = \lambda\sqrt{h^2+k^2+l^2} \,/\, 2\sin\theta,$$

where d_{hkl} is the interplanar spacing, θ is the diffraction angle, and λ is the wavelength of X-ray radiation (0.1542 nm). The main diffraction peak (110) was selected for the calcu-

lation, and the diffraction angles were 36.59° and 37.22°. The calculated lattice constants were 0.3472 nm for specimens V=3 (3-2, 3, 4) and 0.3417 nm for specimens V=2 (2-2, 3). The calculated lattice constants were quite different from any one element in this alloy, which may confirm the occurrence of lattice distortion.

It is noteworthy that the preferred orientation changed from (110) to (200) in specimens 3-3 and 3-4. Correspondingly, the morphologies were quite different for the two specimens, as shown in Figure 3. For alloy coatings fabricated by magnetron sputtering, the development of different preferred orientations has been explained on the basis thermodynamic or kinetic mechanisms [32]. Yang et al. [33] reported that as the thickness decreased, the strain energy of the alloy films also decreased and was accompanied by the optimal orientation shifting to (200). A similar result was reported in other work [34]. For specimens 3-3 and 3-4, with faceted surface features, the thicknesses were lower than those of other alloys. As such, both the 3-3 and 3-4 alloys had lower internal stress, causing the preferred orientation to change from (110) to (200).

3.5 Electrochemical behavior in PBS

Figure 9 shows the potentiodynamic polarization curves of $Ti_{34}Zr_{52}Nb_{14}$ alloy in PBS at room temperature; this alloy possessed the lowest Young's modulus in the work. As shown in Figure 9, the corrosion potential (E_{corr}) and passive current density (I_{corr}) of the alloy were −0.38 V and 0.57 μA/cm^2, respectively. Moreover, the $Ti_{34}Zr_{52}Nb_{14}$ alloy did not exhibit pitting or transpassivation at potentials up to 1 V_{sce}. In comparison, the pitting resistance of $Ti_{34}Zr_{52}Nb_{14}$ was remarkably superior to that of 316L SS and CoCrMo alloys but comparable to that of Ti6Al4V alloys examined in PBS [16]. It should be noted that for an implant in service, pitting corrosion is very harmful to the human body. Generally, it presents a potential failure hazard and the release of metal ions from the implants. In this case, the pitting resistance of the $Ti_{34}Zr_{52}Nb_{14}$ alloy under PBS is remarkably superior to that of 316L SS and CoCrMo alloys.

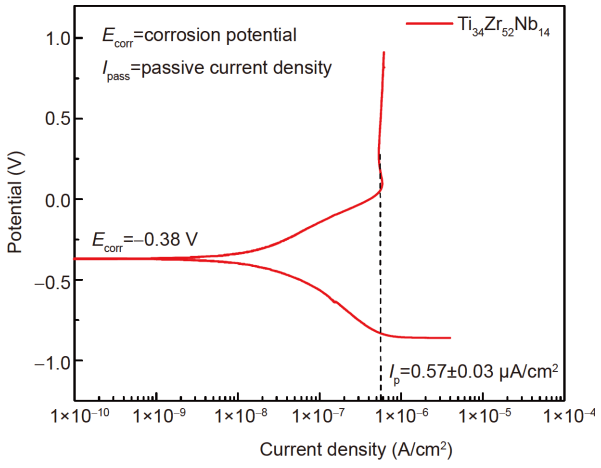

Figure 9 (Color online) Potentiodynamic polarization curves of $Ti_{34}Zr_{52}Nb_{14}$ in PBS.

4 Discussion

4.1 Validity of empirical approach for phase formation prediction

In a multicomponent system, there are several semi-empirical approaches for predicting the solid-solution formation. In most cases, these have been discussed on the basis of "Hume-Rothery" rules. For binary alloys, it has proposed that atom size, electronegativity, and valence electron concentration (VEC) affect solid-solution formation. However, for multi-component alloys, the solutes and solvents are indistinguishable. It is difficult to analyze solid-solution formation by traditional methods. Zhang et al. [30,35] extended the "Hume-Rothery" rules to multi-component alloys and proposed "Ω-δ" rules, which mainly contained three parameters: atomic radius difference (δ), ΔH_{mix}, and ΔS_{mix}. The calculation methods are as follows:

$$\Omega = \frac{T_m \Delta S_{mix}}{|\Delta H_{mix}|},$$

$$\delta = \sqrt{\sum_{i=1}^{n} c_i (r_i - \bar{r})^2},$$

among them,

$$\Delta H_{mix} = \sum_{i=1, i\neq j}^{n} 4 H_{AB}^{mix} c_i c_j,$$

$$\Delta S_{mix} = -R \sum_{i=1}^{n} (c_i \ln c_i),$$

$$T_m = \sum_{i=1}^{n} c_i (T_m)_i,$$

$$\bar{r} = \sum_{i=1}^{n} c_i r_i,$$

where c_i, r_i, and $(T_m)_i$ are the atomic percentage, atom radius, and melting point of the ith component of the alloy, respectively. It is claimed that the formation region of a multi-component solid-solution is Ω≥1.1 and δ≤6.6. For the Ti-Zr-Nb system alloys, the parameters of the constituent elements are listed in Table 2. The δ, ΔH_{mix}, and ΔS_{mix} values of specimens 2-2, 2-3, 3-2, 3-3, and 3-4 are listed in Table 3. It can be concluded that all values of δ and Ω satisfy the criteria for the formation of the solid-solution phase. Such a response is also consistent with the XRD pattern results.

Guo et al. [36] proposed a relationship between VEC and solid-solution stability for multi-component alloys. It should be noted that the VEC parameter can only predict phase stability of either FCC or BCC solid-solution in multi-

Table 3 δ, ΔH_{mix}, ΔS_{mix}, and VEC values of specimens with lower Young's moduli

Specimen	δ (%)	ΔH_{mix} (kJ/mol)	ΔS_{mix} (J/K/mol)	T_m (K)	Ω	VEC
2-2	4.98%	1.33	8.21	2121	13.09	1.87
2-3	5.18%	2.17	8.9	2203	9.04	1.77
3-2	5.14%	1.19	7.77	2126	13.88	1.90
3-3	5.24%	1.98	8.16	2191	9.03	1.82
3-4	5.35%	2.63	8.33	2249	7.12	1.75

component alloys; it cannot be used for predicting the formation ability of the solid-solution phase. On the basis of "Ω-δ" rules predicting the formation ability of the solid-solution phase, the VEC rule is used to test and verify which type of solid-solution phase is stable in these alloys. The VEC parameters are defined as follows:

$$VEC = \sum_{i=1}^{n} c_i (VEC)_i,$$

where $(VEC)_i$ is the valence electron concentration of the ith component of the alloy. It is suggested that FCC phases are more stable at $VEC \geq 8$, whereas BCC phases are more stable at $VEC < 6.78$. For the current Ti-Zr-Nb alloys, the VEC values ranged from 1.5 to 2, which located in the BCC stable area. The above calculations suggest that the Ti-Zr-Nb alloys tend to form a single BCC solid-solution structure, which is consistent with the experimental results.

4.2 Advantages over current orthopedic alloys

A low Young's modulus is fundamental in the screening of biomedical materials. As is well known, replaced prostheses are subject to complex stresses from their surroundings; therefore, a large difference in Young's modulus between the bone and an implant will cause "stress shielding". Typical biomedical metal materials mainly consist of medical stainless steel, cobalt-based alloys, and titanium alloys. Recently, BMG and CEAs have shown potential as biomedical materials. The Young's moduli of these conventional and potential biomedical materials are shown in Figure 10. It is obvious that the Young's moduli are relatively higher than that of human bone. Among the materials, Zn-based and Mg-based BMG have relatively low moduli, close to that of bone. However, they also exhibit relatively low strength, meaning they do not satisfy the requirements of complex stress environments. Taking TiZrNbTa and $(TiZrNbTa)_xMo_{100-x}$ alloys as representatives of CEAs, the Young's moduli range from 110 to 153 GPa [16,27]. However, it cannot be ignored that CEAs usually have very good high compressive strength and excellent corrosion resistance in simulated physiological media.

In this work, the Ti-Zr-Nb system alloys were screened for five compositions that possessed low Young's moduli. In

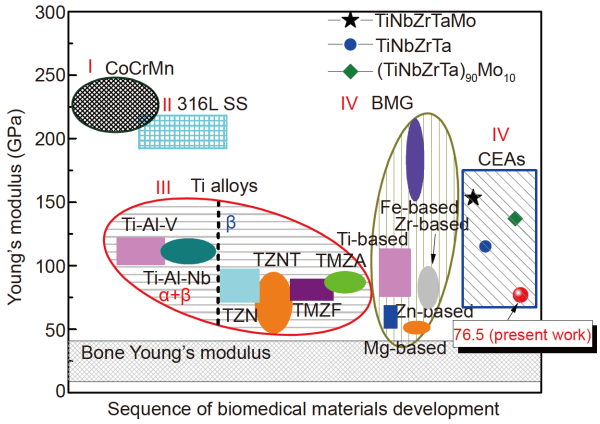

Figure 10 (Color online) Conventional biomedical materials. Abbreviations: TZN: Ti-Zr-Nb, TZNT: Ti-Zr-Nb-Ta, TMZF: Ti-Mo-Zr-Fe, TMZA: Ti-Mo-Zr-Al, CEAs: Configuration entropy alloys.

further composition optimization, the medium entropy alloy $Ti_{34}Zr_{52}Nb_{14}$ exhibited the lowest Young's modulus and indentation hardness (76.5 and 3.8 GPa, respectively). In comparison with conventional alloys, the $Ti_{34}Zr_{52}Nb_{14}$ alloy in the present work had a relatively low Young's modulus and high strength.

It is worth noting that wear resistance is another critical issue for implants with a bearing surface. As indicated by Hertz's contact mechanics, a higher Young's modulus of a material scales with better wear resistance [37]. In this regard, the $Ti_{34}Zr_{52}Nb_{14}$ alloy possesses an ideal Young's modulus value, which is significantly lower than that of typical alloys and higher than those of Mg-based and Zn-based BMGs, as shown in Figure 10. Therefore, good wear resistance is guaranteed with a moderate Young's modulus. Furthermore, $Ti_{34}Zr_{52}Nb_{14}$ exhibited excellent corrosion resistance without any pitting in PBS at anodic potentials up to 1 V_{sce}. Based on previous work, such a response is highly similar to that of Ti_6Al_4V, and significantly better than those of 316L SS and CoCrMo alloys. This indicates that the alloy is less likely to cause failure and ion release via pitting. These advantages of the mechanical and corrosion properties offer the promise of prolonged life of orthopedic implants.

5 Conclusions

By combining multi-target co-sputtering with physical masking, the parallel preparation of Ti-Zr-Nb alloys was studied. Sixteen specimens with different compositions were fabricated. Based on preliminary investigation of this alloy, several issues were highlighted, as follows:

(1) Three typical topographic features were observed in the Ti-Zr-Nb alloys: 1) pyramid-shaped surface features having the cross-section of a columnar structure, 2) spherical-shaped surface features having the cross-section of a granular

structure, and 3) faceted surface features having the cross-section of a lamellar structure.

(2) The Young's modulus and nanoindentation hardness of the specimens ranged from 80.3 to 94.8 GPa and 3.6 to 5.0 GPa, respectively. A lower Young's modulus region, consisting mainly of five specimens, was confirmed within the global system. In further composition optimization, the $Ti_{34}Nb_{52}Zr_{14}$ alloy exhibited the lowest Young's modulus of 76.5 GPa.

(3) The phase structure of the five Ti-Zr-Nb alloys having lower Young's moduli was a single BCC phase. There were two lattice parameters of 0.3417 and 0.3472 nm, which were very different from the lattice parameters of the component elements in the alloy, reflecting the occurrence of lattice distortion. The preferred orientation changed from (110) to (200), mainly due to the change in internal stress caused by the different thicknesses.

(4) The $Ti_{34}Nb_{52}Zr_{14}$ alloy exhibited excellent corrosion resistance in PBS. Compared with 316L SS and CoCrMo alloys, the pitting resistance was significantly improved, indicating that the alloy is less likely to cause failure and ion release by pitting.

In summary, preliminary studies on Ti-Zr-Nb alloys have shown many significant advantages as potential implant materials. This fabrication process also provides a new direction for the parallel preparation of biomedical materials. Further optimization of mechanical properties such as fatigue, wear-resistance, and fracture toughness will be the focus of future work. Moreover, the biological antibacterial properties will need to be verified in future work.

This work was supported by the National Natural Science Foundation of China (Grant No. 51671020).

1 D. C. Ludwigson, Metal Eng. **5**, 1 (1965).
2 M. Navarro, A. Michiardi, O. Castaño, and J. A. Planell, J. R. Soc. Interface **5**, 1137 (2008).
3 R. M. Pilliar, *Metallic Biomaterials* (Springer, New York, 2009), p. 41.
4 M. Geetha, A. K. Singh, R. Asokamani, and A. K. Gogia, Prog. Mater. Sci. **54**, 397 (2009).
5 E. Eisenbarth, D. Velten, M. Müller, R. Thull, and J. Breme, Biomaterials **25**, 5705 (2004).
6 J. Fornell, E. Pellicer, N. Van Steenberge, S. González, A. Gebert, S. Suriñach, M. D. Baró, and J. Sort, Mater. Sci. Eng.-A **559**, 159 (2013).
7 K. Y. Xie, Y. Wang, Y. Zhao, L. Chang, G. Wang, Z. Chen, Y. Cao, X. Liao, E. J. Lavernia, R. Z. Valiev, B. Sarrafpour, H. Zoellner, and S. P. Ringer, Mater. Sci. Eng.-C **33**, 3530 (2013).
8 J. Fornell, N. Van Steenberge, A. Varea, E. Rossinyol, E. Pellicer, S. Suriñach, M. D. Baró, and J. Sort, J. Mech. Behav. Biomed. Mater. **4**, 1709 (2011).
9 N. Chen, X. Shi, R. Witte, K. S. Nakayama, K. Ohmura, H. Wu, A. Takeuchi, H. Hahn, M. Esashi, H. Gleiter, A. Inoue, and D. V. Louzguine, J. Mater. Chem. B **1**, 2568 (2013).
10 W. S. Lee, C. F. Lin, T. H. Chen, and H. H. Hwang, J. Mech. Behav. Biomed. Mater. **1**, 336 (2008).
11 D. Velten, K. Schenk-Meuser, V. Biehl, H. Duschner, and J. Breme, Z. Metallk. **94**, 667 (2003).
12 S. Tamilselvi, V. Raman, and N. Rajendran, Electrochim. Acta **52**, 839 (2007).
13 A. Guitar, G. Vigna, and M. I. Luppo, J. Mech. Behav. Biomed. Mater. **2**, 156 (2009).
14 M. Semlitsch, F. Staub, and H. Weber, Biomed. Tech/Biomed. Eng. **30**, 334 (1985).
15 M. V. Popa, I. Demetrescu, E. Vasilescu, P. Drob, A. S. Lopez, J. Mirza-Rosca, C. Vasilescu, and D. Ionita, Electrochim. Acta **49**, 2113 (2004).
16 S. P. Wang, and J. Xu, Mater. Sci. Eng.-C **73**, 80 (2017).
17 D. Q. Martins, W. R. Osório, M. E. P. Souza, R. Caram, and A. Garcia, Electrochim. Acta **53**, 2809 (2008).
18 M. Geetha, A. K. Singh, K. Muraleedharan, A. K. Gogia, and R. Asokamani, J. Alloys Compd. **329**, 264 (2001).
19 E. Bertrand, T. Gloriant, D. M. Gordin, E. Vasilescu, P. Drob, C. Vasilescu, and S. I. Drob, J. Mech. Behav. Biomed. Mater. **3**, 559 (2010).
20 R. Banerjee, S. Nag, J. Stechschulte, and H. L. Fraser, Biomaterials **25**, 3413 (2004).
21 Y. L. Hao, S. J. Li, S. Y. Sun, C. Y. Zheng, and R. Yang, Acta Biomater. **3**, 277 (2007).
22 J. J. Oak, D. V. Louzguine-Luzgin, and A. Inoue, J. Mater. Res. **22**, 1346 (2007).
23 S. L. Zhu, X. M. Wang, F. X. Qin, and A. Inoue, Mater. Sci. Eng.-A **459**, 233 (2007).
24 Y. Liu, Y. M. Wang, H. F. Pang, Q. Zhao, and L. Liu, Acta Biomater. **9**, 7043 (2013).
25 J. W. Yeh, JOM **65**, 1759 (2013).
26 Y. D. Wu, Y. H. Cai, T. Wang, J. J. Si, J. Zhu, Y. D. Wang, and X. D. Hui, Mater. Lett. **130**, 277 (2014).
27 S. P. Wang, and J. Xu, Intermetallics **95**, 59 (2018).
28 Y. Zhang, X. H. Yan, J. Ma, Z. P. Lu, and Y. H. Zhao, J. Mater. Res. **33**, 3330 (2018).
29 X. H. Yan, J. S. Li, W. R. Zhang, and Y. Zhang, Mater. Chem. Phys. **210**, 12 (2017).
30 Y. Zhang, Z. P. Lu, S. G. Ma, P. K. Liaw, Z. Tang, Y. Q. Cheng, and M. C. Gao, MRS Commun. **4**, 57 (2014).
31 International Organization for Standardization. *Metallic Materials-Instrumented Indentation Test for Hardness and Materials Parameteres-Part 1: Test Method*, BS EN ISO 14577-1: 2002 (2002).
32 J. Pelleg, L. Z. Zevin, S. Lungo, and N. Croitoru, Thin Solid Films **197**, 117 (1991).
33 H. H. Yang, J. H. Je, and K. B. Lee, J. Mater. Sci. Lett. **14**, 1635 (1995).
34 L. J. Meng, and M. P. Santos, Surf. Coatings Tech. **90**, 64 (1997).
35 X. Yang, and Y. Zhang, Mater. Chem. Phys. **132**, 233 (2012).
36 S. Guo, C. Ng, J. Lu, and C. T. Liu, J. Appl. Phys. **109**, 103505 (2011).
37 H. Hertz, J. Reine Angew. Math. **92,** 156 (1881).